# Electronic Supplementary Information (ESI)

# Upcycling Plastic Waste into Fully Recyclable Composites through Cold Sintering

Po-Hao Lai [a], Shelby L. Hall [a], Yi-Chen Lan [a], Jia-Ruey Ai [a], Arian Jaberi [a], Amir Sheikhi [a], Rui Shi [a], Bryan D. Vogt[*a], and Enrique D. Gomez[*ab]

[a] *Department of Chemical Engineering, The Pennsylvania State University, University Park, PA 16802, USA.*

[b] *Department of Material Science and Engineering, The Pennsylvania State University, University Park, PA 16802, USA.*

*e-mail: bdv5051@psu.edu, edg12@psu.edu

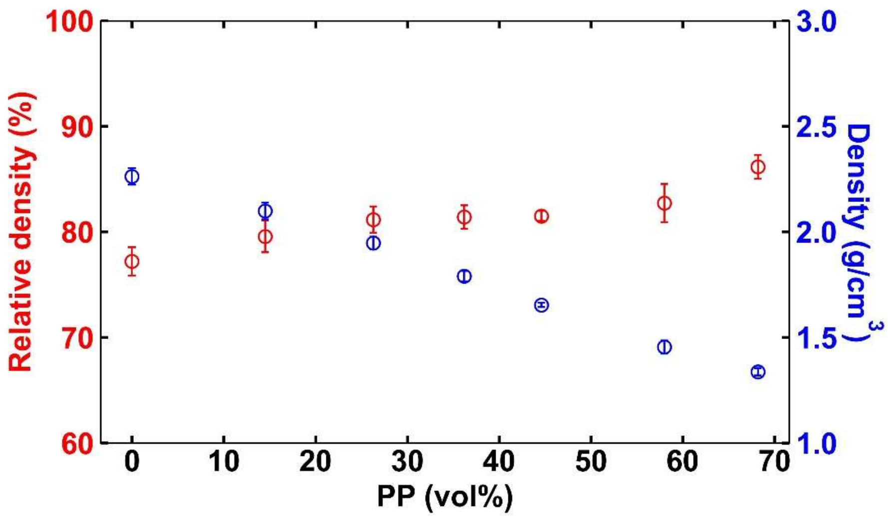


**Fig. S1.** Relative density (red) and the measured density (blue) of $CaSO_4$/PP composites. Relative density is calculated by dividing the measured density by the maximum theoretical density at each given composition and expressed as a percentage (x100). The theoretical density $\rho_T$ is calculated based on the volume fractions $v_1$, $v_2$, and maximum densities of individual components $\rho_1$, $\rho_2$ as $\rho_T = \rho_1\ v_1 + \rho_2\ v_2$. The relative density provides a clear comparison of densification between samples as the density will vary based on composition due to the difference in density between $CaSO_4$ and PP.

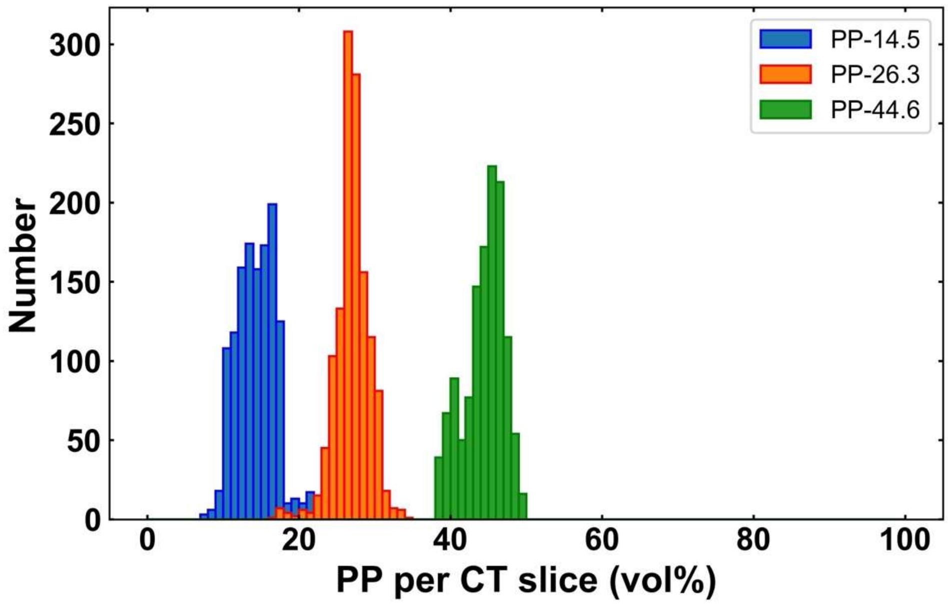

**Fig. S2.** Histogram of local composition of cross-sections from μCT analysis for $CaSO_4$/PP composites.

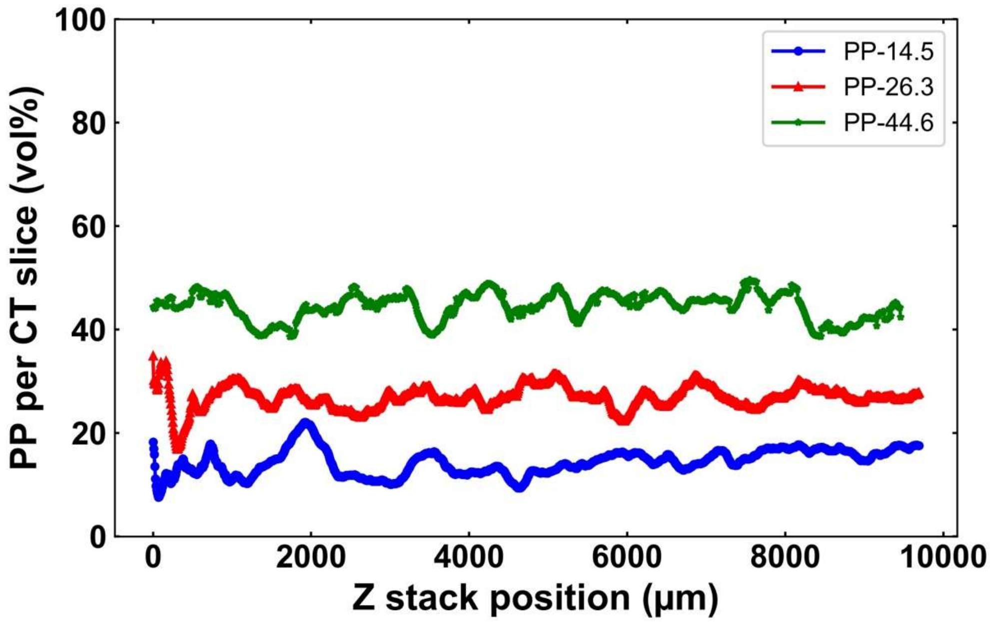


**Fig. S3.** PP content from each cross-section of μCT reconstuctions for $CaSO_4$/PP composites along the length of the tensile bars.

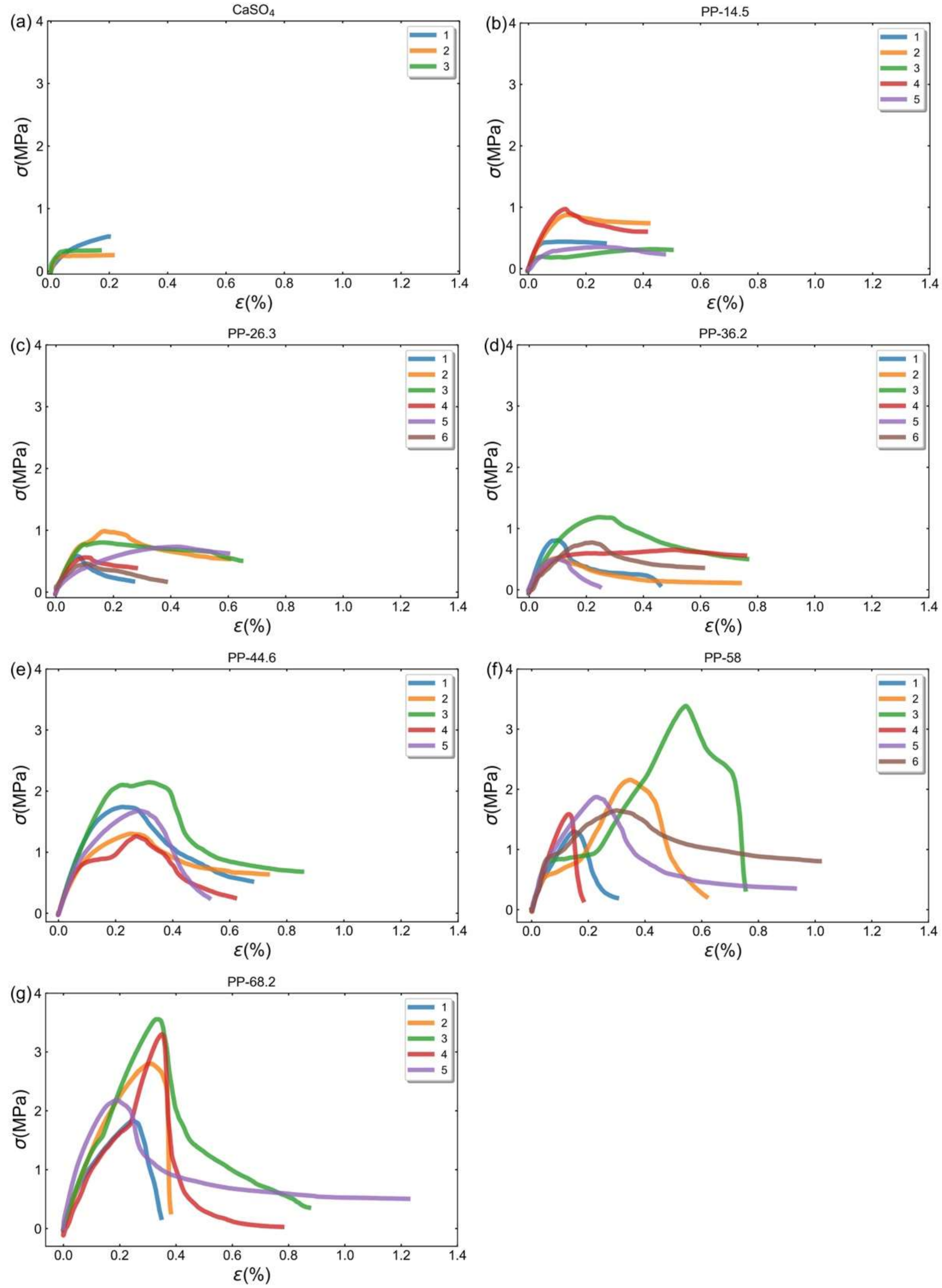


**Fig. S4.** Stress-strain curves of all cold sintered $CaSO_4$/PP composites: (a) $CaSO_4$, (b) PP-14.5, (c) PP-26.3, (d) PP-36.2, (e) PP-44.6, (f) PP-58, and (g) PP-68.2.

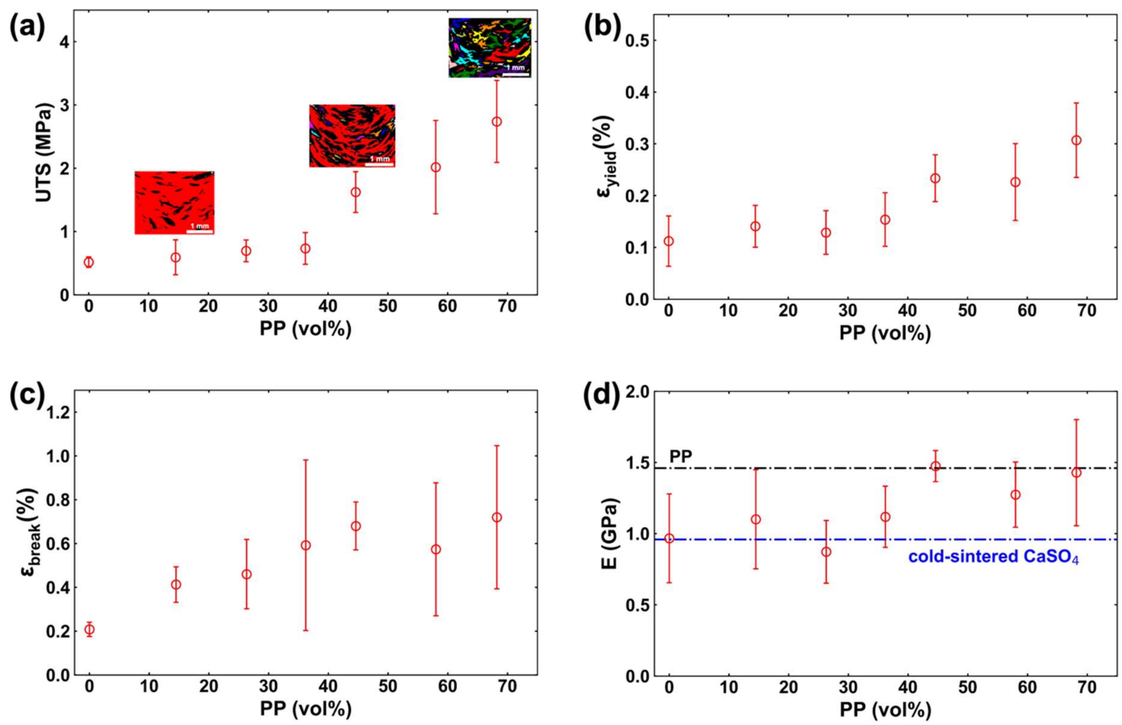


**Fig. S5**. Tensile properties of the cold sintered $CaSO_4$/PP composites: (a) ultimate tensile strength, (b). elongation at yield, (c). elongation at break and (d) Young's modulus. The inset images in (a) illustrate the morphology of these composites. The dashed lines in (d) provide the Young's modulus of the PP from compression molding and the pure $CaSO_4$ after cold sintering for comparison.

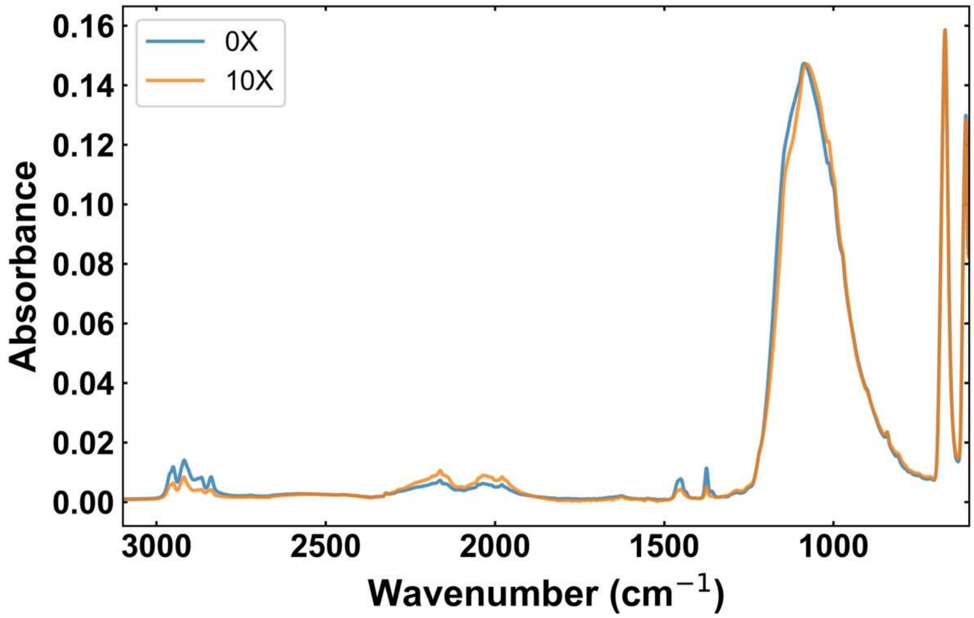


**Fig. S6.** FTIR spectra of the pristine $CaSO_4$/PP 44.6 composite (0X) and $CaSO_4$/PP 44.6 composite after reprocessing 10 times (10X).

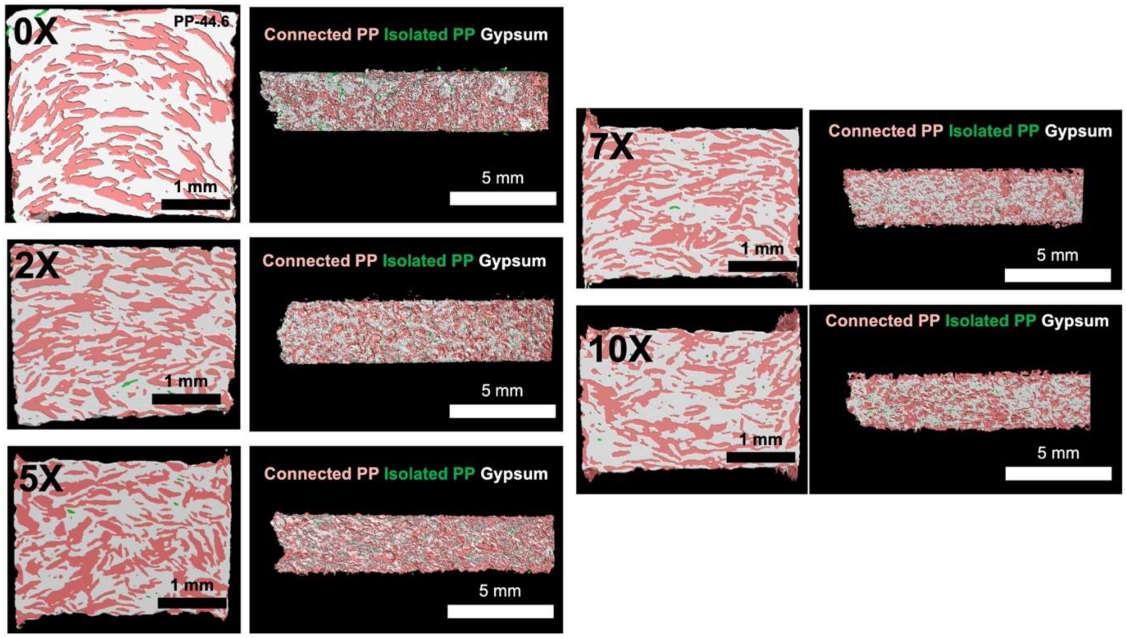


**Fig. S7.** Connectivity analysis of μ-CT images for PP-44.6 at different recycle steps.

**Table S1. Composition and connectivity of PP-44.6 at different recycle steps from μ-CT analysis.**

| | Pristine | R-2 | R-5 | R-7 | R-10 |
|---|---|---|---|---|---|
| **PP fraction (%)** | 47.9 ± 5.1 | 46.3 ± 2.9 | 45.4 ± 2.8 | 45.6 ± 3.5 | 44.3 ± 5.6 |
| **PP connectivity (%)** | 99.7 ± 0.2 | 99.7 ± 0.1 | 99.6 ± 0.3 | 99.7 ± 0.1 | 99.6 ± 0.2 |
| **$CaSO_4$ thickness (μm)** | 102.2 ± 26.7 | 86.76 ± 21.3 | 92.8 ± 22.8 | 76.9 ± 24.6 | 77.8 ± 13.4 |

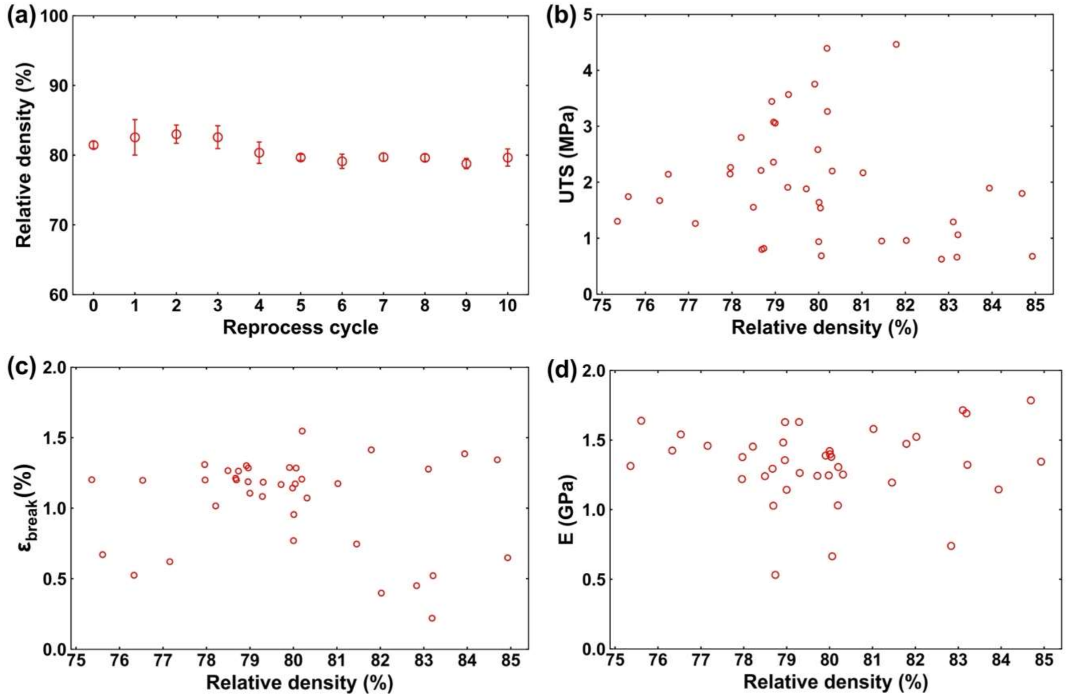


**Fig. S8.** (a) Dependence of the relative density of PP-44.6 on recycling. The relative density does not appear to be strongly correlated with the (b) ultimate tensile strength, (c) elongation at break, and (d) Young's modulus. Each data point is a distinct sample and all samples measured are shown in the plots.

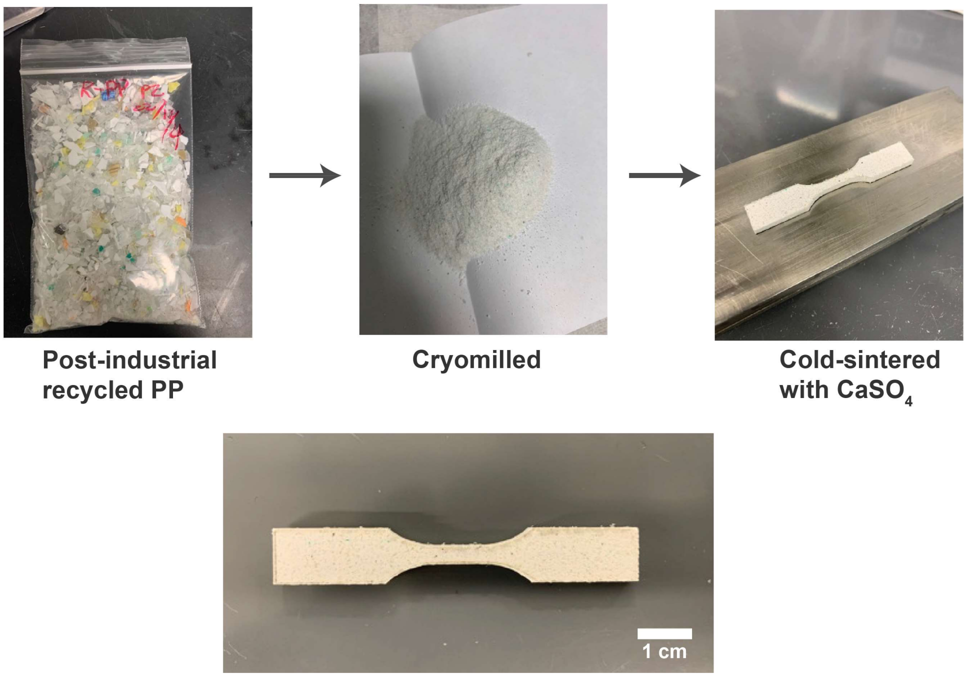


**Fig. S9.** Schematic for the process to fabricate Waste-PP-44.6 composite.

**Table S2. Tensile properties comparison between PP-44.6 and Waste-PP-44.6**

| | UTS (MPa) | YM (GPa) | Elongation at yield (%) | Elongation at break (%) |
|---|---|---|---|---|
| **PP-44.6** | 1.62 ± 0.32 | 1.47 ± 0.11 | 0.24 ± 0.05 | 0.84 ± 0.30 |
| **Waste-PP-44.6** | 1.50 ± 0.18 | 0.65 ± 0.12 | 0.28 ± 0.02 | 1.34 ± 0.18 |

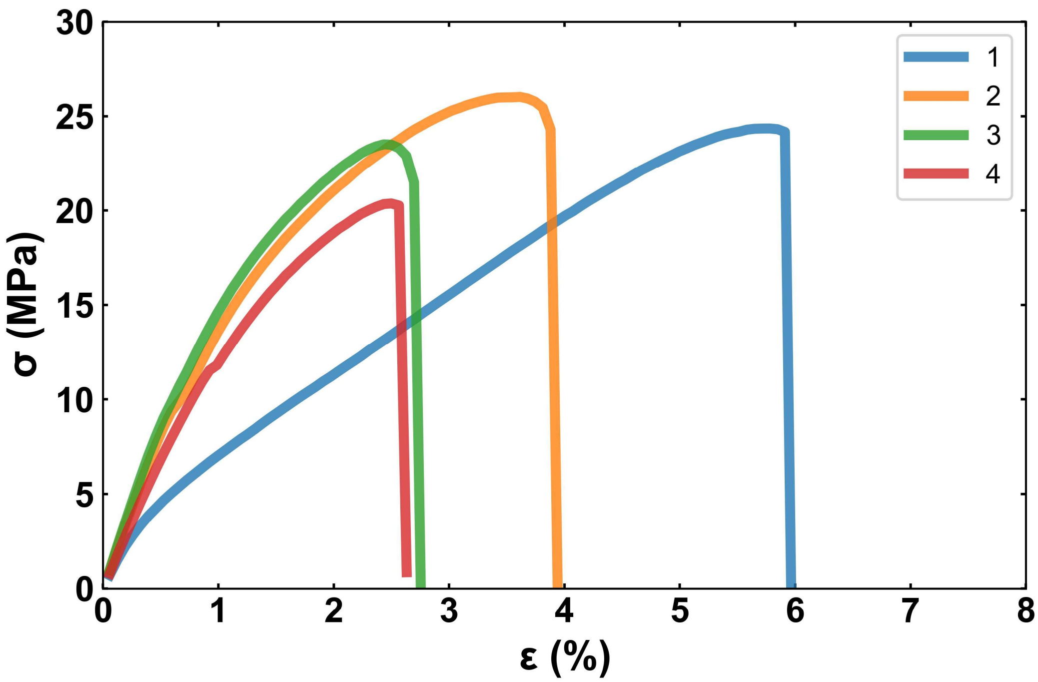


**Fig. S10.** Stress-strain curves of compression molded tensile bar of waste PP (post-industrial recycled). The different lines correspond to different specimens (n=4) tested.

**Table S3. Tensile properties comparison between virgin PP and waste PP (post-industrial recycled)**

| | UTS (MPa) | YM (GPa) | Elongation at yield (%) |
|---|---|---|---|
| **Virgin PP*** | 34.7 | 1.46 | 10 |
| **Waste PP (post-industrial recycled)** | 23.52 ± 2.06 | 0.71 ± 0.20 | 3.52 ± 1.35 |

***Data from Materials Data Sheet (ExxonMobil)**

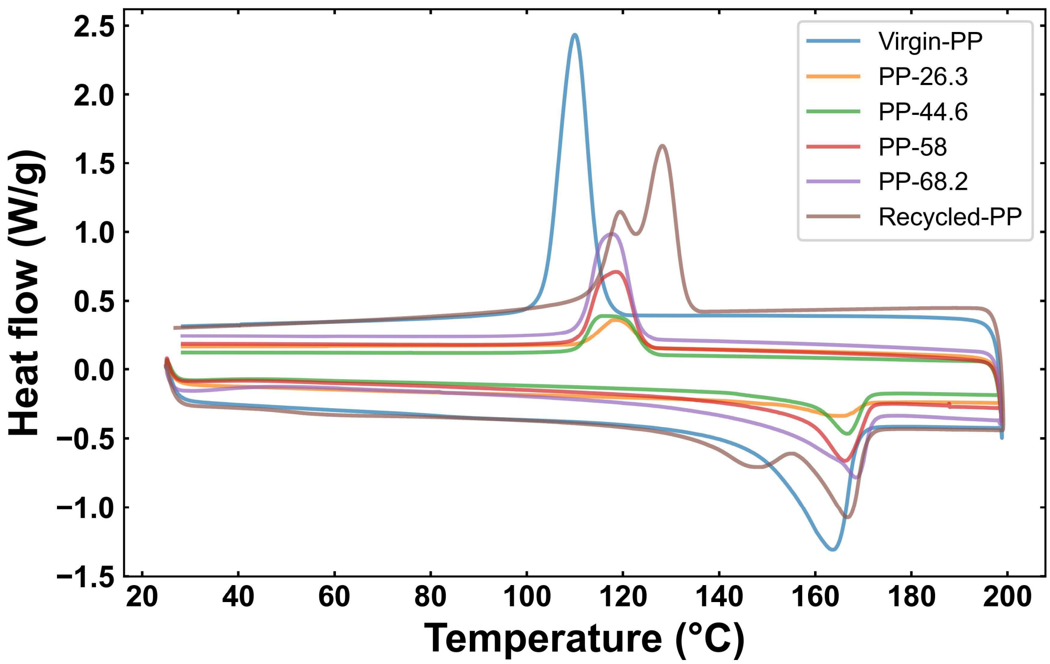


**Fig. S11.** DSC thermograms of Virgin-PP, different $CaSO_4$/PP composites, and Recycled-PP. Exotherm is up for these curves. The heating and cooling rate for the scans was 10 °C/min.

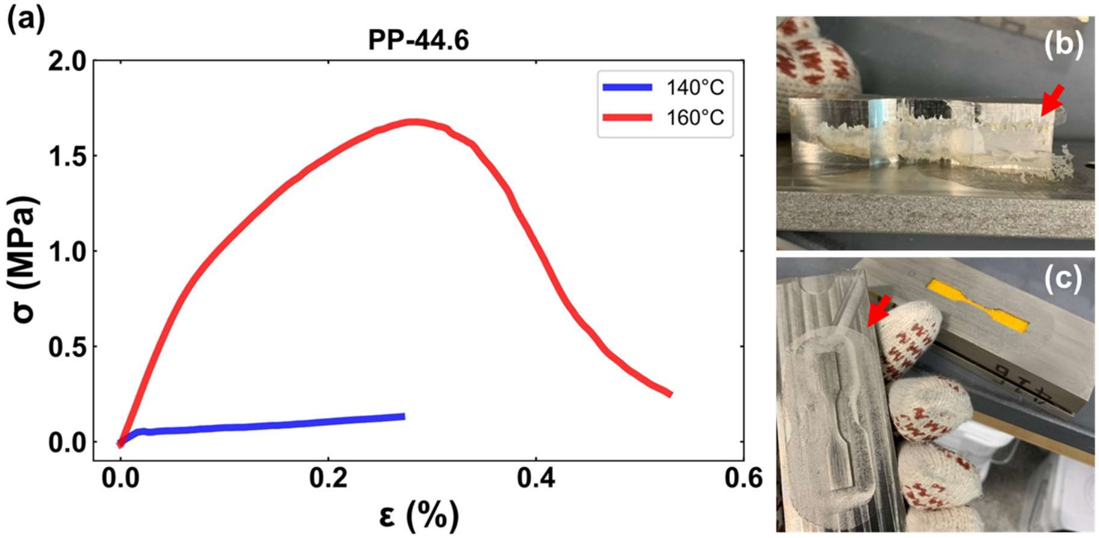


**Fig. S12.** Optimization of cold sintering temperature. Cold sintering of PP-44.6 below 160 $^oC$, such as at 140 $^oC$, prevents PP from melting and composite mechanical properties are substantially decreased. (b) Cold sintering of PP-68.2 at 180 $^oC$ and at (c) 200 $^oC$ for 1 hr leads to leaking of PP out of the mold, as highlighted by the red arrows.

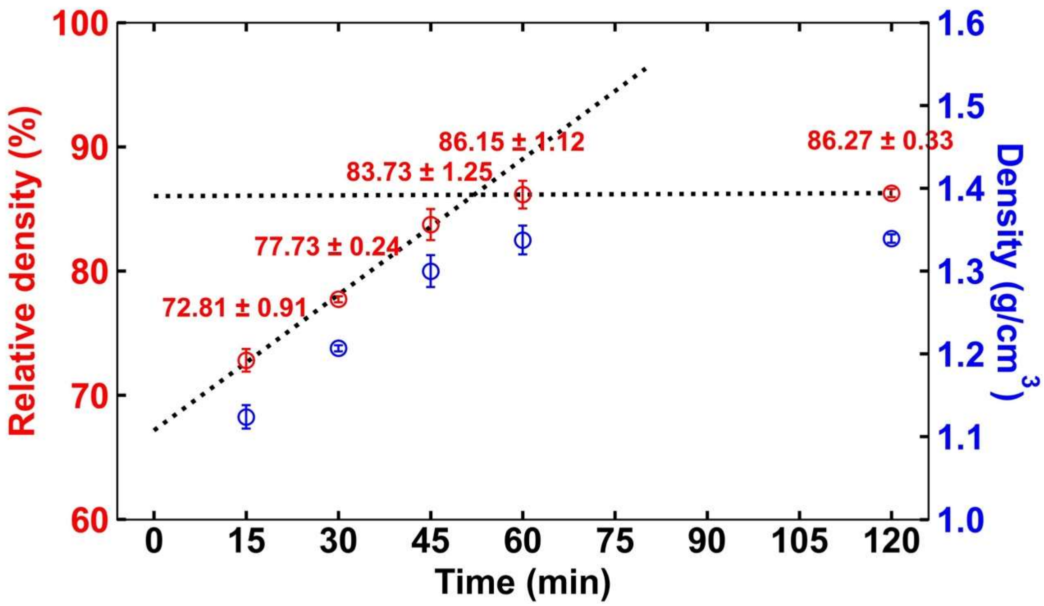


**Fig. S13.** Relative density (red) and the measured density (blue) of PP-68.2 after various cold sintering times when processed at 160 ℃ and 200 MPa.

**Additional experimental details for LCA**

We performed life cycle impact assessment to compare the impact on primary energy demand, global warming potential (GWP), and water demand of our cold sintering process. We compare composites of gypsum and PP-44.6, including when waste PP is used, with other structural and building construction materials, including sawn timber (softwood kiln dried), glue laminated timber, particle board, oriental strand board, and drywall (gypsum-based). We calculate energy demand, GWP and water demand using data available from the mining and manufacturing of gypsum and polypropylene. GWP-100 considers the contribution of a greenhouse gas to global warming over 100 years. Because the process is consuming energy from the local grid, information regarding fuel mix breakdown and GWP of the grid was gathered using the eGRID database from EPA.

For calculating the impacts of fabrication of cold sintered composites, the model considers the heat capacity and weight fraction of the components. Additionally, because two components undergo phase changes, the model includes the heat of vaporization for the solvent, and the heat of fusion for the plastic component. Although we expect heat loss to the environment during sintering, we assume this loss to have a minimal impact on energy demand and GWP. Thus, we calculate the heat demand $Q_{in}$ as:

$$Q_{in} = \sum_{n=1}^{3} \omega_n Cp_n\, m_t \Delta T_{12} + \Delta H_{vap} m_{sol} + \Delta H_{fus} m_p + \sum_{n=1}^{3} \omega_n Cp_n\, m_t \Delta T_{23} \qquad (1)$$

where $w$ is weight fraction, $C_p$ is heat capacity in $Jg^{-1}K^{-1}$, $m_t$ is total mass being sintered, $\Delta T_{12}$ is temperature difference in Kelvin from ambient to 100 °C and $\Delta T_{23}$ from 100 to 160 °C, $\Delta H_{vap}$ is heat of vaporization of the solvent, $\Delta H_{fus}$ is the heat of fusion, $m_{sol}$ is the mass of the solvent and $m_p$ is the mass of the plastic. The small pressure coefficient for the boiling point of water is not included as the system is open and water vapor can escape. We thus calculate the primary energy demand as $Q_{in} + W$, where $W$ is the work due to the applied pressure. The inventory analysis was done based on 1 kg of material, and the chosen functional unit was 1 $m^2$ of material (with a thickness of 12.7 mm). Results for Primary energy demand, GWP, and Water demand are shown in Table S4.

**Table S4. Life cycle analyses for comparison with common construction materials: Primary energy demand, Global warming potential (GWP), and Water demand.**

| Building product | Primary energy demand ($J\text{-}Eq/m^2$) | GWP ($kg\ CO_2\text{-}Eq/m^2$) | Water demand ($kgH_2O/m^2$) |
|---|---|---|---|
| **Particle board** | $2.59 \times 10^9$ | 62.2 | 99.1 |
| **Oriented strand board** | $1.58 \times 10^9$ | 32.6 | 66.2 |
| **Glued laminated timber** | $8.72 \times 10^8$ | 28.1 | 133 |
| **Sawn timber** | $5.57 \times 10^8$ | 10.0 | 30.6 |
| **Drywall** | $3.47 \times 10^7$ | 2.23 | 20.0 |
| **Gypsum PP-44.6 board (virgin)** | $1.00 \times 10^7$ | 1.62 | 20.0 |
| **Gypsum PP-44.6 board (recycled)** | $1.40 \times 10^5$ | 0.0120 | 0.100 |